Integrated Graph Cuts for Brain MRI Segmentation

Zhuang Song, Nicholas Tustison, Brian Avants, and James C. Gee

Penn Image Computing and Science Lab, University of Pennsylvania, USA
songz@seas.upenn.edu*

Abstract. Brain MRI segmentation remains a challenging problem in spite of numerous existing techniques. To overcome the inherent difficulties associated with this segmentation problem, we present a new method of information integration in a graph based framework. In addition to image intensity, tissue priors and local boundary information are integrated into the edge weight metrics in the graph. Furthermore, inhomogeneity correction is incorporated by adaptively adjusting the edge weights according to the intermediate inhomogeneity estimation. In the validation experiments of simulated brain MRIs, the proposed method outperformed a segmentation method based on iterated conditional modes (ICM), which is a commonly used optimization method in medical image segmentation. In the experiments of real neonatal brain MRIs, the results of the proposed method have good overlap with the manual segmentations by human experts.

1 Introduction

Accurate and efficient voxel based segmentation of white matter (WM), gray matter (GM), and cerebrospinal fluid (CSF) is essential for quantitative brain image analysis. The main challenge of automatic brain tissue segmentation stems from the problem of the absence of distinct boundaries between different brain tissues. This problem is due to a combination of multiple factors, such as imaging noise, field inhomogeneity, partial volume effect, and intrinsic tissue variation. To overcome these difficulties, it is necessary to integrate complementary information derived from the image as well as prior knowledge [1]. This paper presents a new method of information integration to facilitate the brain tissue segmentation, in a graph based framework [2].

Markov Random Field (MRF) theory provides a sound background to model context dependent image segmentation, in which image segmentation is formulated as a problem of energy minimization. Let $\mathcal{P}$ denotes the set of voxels in the image. The MRF-based energy function describes the total energy associated with assigning each voxel $p \in \mathcal{P}$ one of the labels in the label set $\mathcal{L}$. There are various forms of energy functions to model specific image segmentation problems. Finding the energy minimum yields the desired image segmentation. A

* This work was supported in part by the USPHS under grants DA-015886, MZ-402069, NS-045839, and MH-072576.

R. Larsen, M. Nielsen, and J. Sporring (Eds.): MICCAI 2006, LNCS 4191, pp. 831–838, 2006.

successful image segmentation depends crucially on both the formulated energy function and the optimization method. Let an image be denoted by I, a defined neighborhood system by $\mathcal{N}$, and the labeling on the image by f, the MRF-based energy function has the basic form given by

$$E_I(f) = \lambda \sum_{p \in \mathcal{P}} D_p(f_p) + \sum_{\{p,q\} \in \mathcal{N}} V_{p,q}(f_p, f_q), \tag{1}$$

where the data term $D_p(f_p)$ is a function derived from the observed data and measures how well the label f_p can be assigned to the voxel p based on a chosen probabilistic model. The smoothness term $V_{p,q}(f_p, f_q)$ measures the neighborhood interaction by penalizing discontinuities between the voxel pair $\{p, q\}$ in a specified neighborhood system $\mathcal{N}$. The coefficient λ weights the relative contribution between the data term and the smoothness term.

For an MRF-based energy function, global optimization methods, such as Gibbs Sampler [3], are often computationally too inefficient to be applicable to 3D medical image segmentation. On the other hand, iterated conditional modes (ICM) [4], a deterministic optimization method which has been widely applied to medical image segmentation, is well known to suffer from local minima trapping [5]. The graph cut method is a relatively recent development in minimizing context-dependent MRF problems [2,6]. It has been proven to be able to locate global minima for a certain class of two-label energy functions [5,7]. Although global minimization is NP-hard for multi-label energy functions, the graph cut method can guarantee strong approximation to global minima [2]. In the graph formulation, the MRF-based energy function in Equ.(1) is coded into the edge weights. The cost of graph cut is equal to the total energy of the corresponding segmentation.

To address the specific problems in brain MRI tissue segmentation, we propose an automatic brain tissue segmentation method based on the multi-label graph cut method described in [2]. Our method integrates intensity, local boundary information, and tissue priors into the edge weight metrics. In addition, inhomogeneity correction is incorporated in the adaptive graph construction. This is done by updating the edge weights according to the intermediate inhomogeneity field estimation. The proposed method was validated on both simulated and real brain MRIs.

2 Method

The binary graph cut method and the extension to multi-label graph cuts by the α-expansion algorithm are described in [6] and [2], respectively. Given an image with a set of voxels $\mathcal{P}$, the goal of segmentation is to partition $\mathcal{P}$ into $\mathcal{K}$ disjoint sets $\mathcal{P}_i$, *i.e.*, $\mathcal{P} = \bigcup_{i=1}^{\mathcal{K}} \mathcal{P}_i$ and $\mathcal{P}_i \bigcap \mathcal{P}_j = \emptyset$, if $i \neq j$. For the proposed algorithm, the image is represented by a weighted graph, $\mathcal{G} = \langle \mathcal{V}, \mathcal{E} \rangle$, where the set of nodes is denoted by $\mathcal{V} = \mathcal{P} \bigcup \mathcal{L}$. $\mathcal{L}$ denotes the set of terminal nodes which represents the labels. The set of edges is denoted by $\mathcal{E} = \mathcal{E}_{\mathcal{N}} \bigcup \mathcal{E}_{\mathcal{T}}$, where $\mathcal{E}_{\mathcal{N}}$ denotes the set of voxel-to-voxel edges in the defined neighborhood system

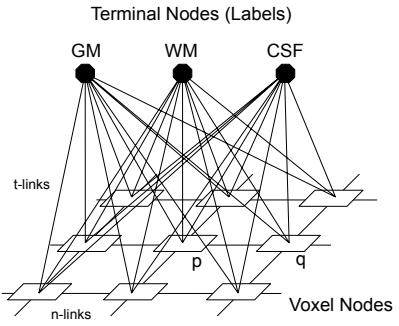

Fig. 1. Example of the graph with three terminals for brain MRI tissue segmentation of gray matter (GM), white matter (WM), and cerebrospinal fluid (CSF). The set of nodes $\mathcal{V}$ includes all voxels and terminals.The set of edges $\mathcal{E}$ includes all n-links and t-links.

(n-links) and $\mathcal{E}_{\mathcal{T}}$ denotes the set of voxel-to-terminal edges (t-links). A typical graph construction for brain tissue segmentation is illustrated in Fig.1, where the three terminal nodes refer to the three brain tissue types. The set of edges $\mathcal{E}$ can be formulated such that a segmentation derived from the solution of the graph cut algorithm [2] minimizes certain MRF-based energy functions. In the graph construction, $D_p(\cdot)$ in Equ.(1) describes the edge weights of the t-links, whereas $V_{p,q}(\cdot)$ describes the edge weights of the n-links. A graph cut $\mathcal{C} \in \mathcal{E}$ is a set of edges such that the linked nodes are in disjoint sets while each voxel node has to connect with only one terminal node which corresponds to its label. The resulting graph is denoted by $\mathcal{G} = \langle \mathcal{V}, \mathcal{E} - \mathcal{C} \rangle$. The cost of the cut $|\mathcal{C}|$ is the sum of its edge weights in the edge set $\mathcal{C}$.

2.1 Information Integration in Edge Weight Metrics

In this graph cut method, t-links are the major force in segmentation, while n-links enforce smoothness in a specified neighborhood. Intensity is the primary voxel-wise image feature used to define the edge weight metrics for both t-links and n-links. Generally the weights of t-links $\mathcal{E}_{\mathcal{T}}$ are derived from a certain probabilistic model according to the intensity distribution of each tissue type in the image, and the weights of n-links are derived from the similarity measured between nodes. To cope with the complexity and variability in brain MRI, prior knowledge of brain anatomy and tissue properties is an important resource to be integrated into automatic segmentation. Furthermore it is well understood that the intensity-based methods are susceptible to field inhomogeneity in MRIs [1]. Local boundary information provides complementary information which helps to detect the actual boundary between different tissues. In the following section, we describe the integration of tissue priors, local boundary information, and intensity information in the edge weight metrics.

Integration of Tissue Priors in T-Links. To integrate prior knowledge of brain tissues, the MRF energy function given in Equ.(1) is reformulated to include the atlas-based prior knowledge which becomes

$$E(f) = \gamma E_I(f) + (1-\gamma)E_A(f), \tag{2}$$

where the new energy $E(f)$ is biased by the atlas-based energy term $E_A(f)$, and the user-selected parameter, $\gamma \in [0,1]$, moderates the two terms and is derived empirically. The atlas-based energy E_A is derived from the probabilistic atlas priors, which are generated by registering a sufficient number of pre-segmented MRIs to a canonical atlas space. Trained individuals segment brain tissues on each of the MRIs used in the atlas construction. Effective atlas construction relies on a robust inter-subject registration method. A symmetric diffeomorphic flow-based registration method was used [8]. The prior probability that a voxel is assigned a label is estimated by averaging the manual labeling of that voxel over the set of registered MRIs within the canonical atlas space. This average is denoted as P_A. The energy contribution from each voxel labeling is defined as

$$E_A(f_p) = -\ln P_A(f_p), \tag{3}$$

where $f_p \in \mathcal{L}$. Therefore, conjoining Equ.(1), (2), and (3) leads to the following total energy function to be minimized,

$$E(f) = \sum_{p\in\mathcal{P}} \left(\lambda\gamma D_p(f_p) + (1-\gamma)E_A(f_p)\right) + \gamma \sum_{\{p,q\}\in\mathcal{N}} V_{p,q}(f_p, f_q). \tag{4}$$

Based on Equ.(4),the edge weight of t-links in the graph is

$$T_p(L_i) = \lambda\gamma D_p(L_i) + (1-\gamma)E_A(L_i), \tag{5}$$

where $L_i \in \mathcal{L}$, and $D_p(L_i)$ is defined as the negative log-likelihood of the image intensity distribution,

$$D_p(L_i) = -\ln P_I(I_p|L_i), \tag{6}$$

where $P_I(I_p|L_i)$ is estimated by a Gaussian model of the intensity distribution of each tissue type.

Integration of Local Boundary Information in N-Links. Intensity and local boundary information are combined into the calculation of the edge weights of n-links. Image intensity is denoted as I_p for voxel $p \in \mathcal{P}$. The Lorentzian error norm [9], a type of robust metric, is used to measure the intensity difference between two voxel nodes p and q within a neighborhood,

$$\rho(p,q) = \ln\left(1 + \frac{1}{2}\left(\frac{|I_p - I_q|}{\sigma}\right)^2\right),$$

where the robust scale σ can be estimated from the input image [9]. This quantity is used to calculate the intensity-based component of the edge weights of n-links

$$W^R_{p,q} = 1/(1+\rho).$$

The boundary-based component of the n-link edge weight is derived from intervening contour probabilistic map B [10]. This map is computed through a transformation using the gradient image G. For any voxel p, $B_p = 1 - \exp(-G_p/\sigma_G)$, where σ_G is the normalization factor. The probability to have a gradient-based boundary between any two voxels $\{p, q\}$ is defined as the maximal intervening contour probability in the set of voxels along the line joining p and q, denoted as $M_{p,q}$. The boundary-based component of the edge weight of the n-links is thus defined as

$$W^B_{p,q} = 1 - \max_{x \in M_{p,q}} (B_x).$$

Combining the intensity and boundary components, the n-link edge weight metric becomes

$$W_{p,q} = cW^I_{p,q} + (1 - c)W^B_{p,q}, \tag{7}$$

where the coefficient $c \in [0, 1]$ is used to weight the importance of intensity versus boundary information to enforce the edge preserving smoothness. It is noted that $W_{p,q}$ is equivalent to $V_{p,q}(f_p, f_q)$ in Equ.(4) after assigning a label to each voxel.

2.2 Adaptive Inhomogeneity Correction

The adaptive component of the segmentation combines inhomogeneity correction and segmentation in an iterative mode. MRI inhomogeneity is characterized by a low frequency field in the image domain. The inhomogeneity field is assumed to be multiplicative and uniform for any tissue types. Initial intensity means are estimated by the K-d tree based K-means clustering method. Given the intermediate segmentation results, the intensity mean μ_{L_i} of each label L_i is updated. The voxel value in quotient image Q is computed by $Q_p = I_p/\mu_{f_p}$, where I_p denotes the intensity of voxel p, f_p denotes the label assigned to voxel p. The image Q is the input to the field estimation function. A cubic B-spline approximation scheme for scattered data given in [11] is applied to estimate the inhomogeneity field $\mathcal{H}$. The inhomogeneities are corrected by dividing the original image intensity by the estimated inhomogeneity field at each voxel $\mathcal{H}(p)$. This subsequently updates $D_p(L_i)$ of voxel p for every terminal node L_i in the t-link metric in Equ.(5).

3 Experimental Results

The proposed method was validated on both simulated and real brain MRIs. Current implementation of the method is in 2-D. The 3-D image segmentation is processed slice-by-slice, while inhomogeneity correction was performed in the 3-D volume. The 3-D graph cut algorithm has the same formulation except that the neighborhood structure is in 3-D and the computation is thus more expensive. A volumetric overlap metric was used to compare the segmentation results of the proposed method and the ground truth. For each label $\mathcal{L}_i \in \mathcal{L}$, the volumetric overlap metric is defined as

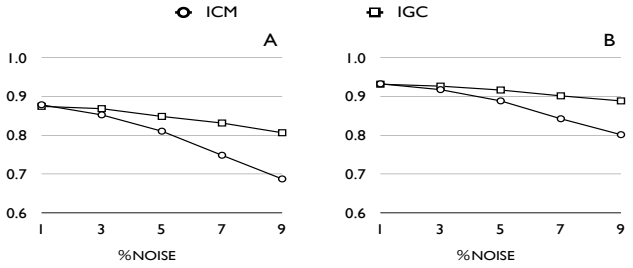

Fig. 2. Overlap metrics for the segmentation of (A) GM and (B) WM of BrainWeb simulated T1 weighted images with 40% field inhomogeneity, using our integrated graph cut algorithm (IGC) and the one in [12] using ICM to minimize the energy function. It is noted that atlas priors are not used in this experiment, and both methods have the component of adaptive inhomogeneity correction.

$$O_{A,B}(\mathcal{L}_i) = \frac{V_{A \bigcap B}(\mathcal{L}_i)}{V_{A \bigcup B}(\mathcal{L}_i)}$$

where $V_{A \bigcap B}(\mathcal{L}_i)$ denotes the number of voxels labeled as $\mathcal{L}_i$ by both the proposed method and the ground truth, and $V_{A \bigcup B}(\mathcal{L}_i)$ denotes the number of voxels labeled as $\mathcal{L}_i$ by either the proposed method or the ground truth.

Simulated images were generated from the BrainWeb MR simulator with 40% field inhomogeneity and 1%-9% noise [13]. The simulated T1-weighted images had voxel dimensions $181 \times 217 \times 181$, with voxel size $1 \times 1 \times 1$ mm. As shown in Fig.2, the graph cuts have stable performance in spite of image noise and field inhomogeneity, and consistently outperforms an ICM based segmentation method [12]. To make a fair comparison, the atlas weight γ in Equ.(2) was set to be zero in this experiment. Atlas priors were used in the following experiment of real images.

The real images used were MRI scans of neonatal brains, which are more difficult than adult brains for tissue segmentation because of its greater intrinsic tissue variation. The neonates used in this study were term newborn infants with the ages less than 10 days when myelination of white matter was at an early stage. Therefore, image intensities of myelinated and non-myelinated white matters were considered to be within the variance range of a single tissue type. It is noted that, in general, a T2-weighted neonatal MRI has better contrast than a T1-weighted MRI. Axial T2-weighted images were scanned by using spin-echo pulse sequence. The image voxel size is $0.35 \times 0.35 \times 3mm$. These images have low contrast-to-noise ratio, large partial volume effect, and exhibit severe field inhomogeneity.

Leave-one-out cross validation was applied to ten T2-weighted brain neonatal MRIs. Gray and white matters in all these MRIs were delineated by two human experts. Skull and other brain tissues were excluded from the images according to the manual delineation. In each round, nine of the ten MRIs were used to generate the probabilistic atlases for gray and white matters. The constructed atlas was then used in the segmentation of the remaining neonate. Fig.3 shows

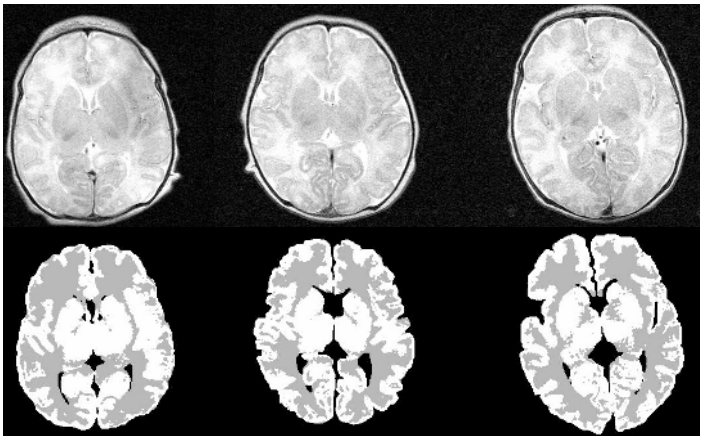

Fig. 3. Example axial slices of T2 weighted brain MRIs of three neonates and the corresponding segmentation results of the proposed method

some example slices of the segmentation results by the proposed method. The segmentation results were compared with the corresponding manual segmentations. The volumetric overlap metric was calculated for gray and white matter respectively, and the results for the ten neonates are summarized in Table 1. As shown in the table, the results of the proposed method for real neonatal images are approximately in the range of inter-rater variance. The construction of the probabilistic atlas is difficult for the low axial resolution and low contrast-to-noise ratio in the image. In addition, the performance of the method can be improved by using a more realistic probabilistic model $D_p(\cdot)$ in Equ.(6).

4 Discussion

This paper describes a new method of information integration in a graph-based framework [2] for brain MRI segmentation. Although the graph cut method has provable capability to minimize energy functions, it requires careful formulation of the edge weight metrics to achieve successful performance for specific problems. In the proposed method, intensity, local boundary information, and tissue priors have been integrated in the edge weight metrics. Moreover image

Table 1. Overlap metrics of the proposed method, the integrated graph cut (IGC), and the manual segmentation for the ten real neonatal brain MRIs. The manual segmentation is derived from the intersection of two manual segmentations by two raters. The second row of the table shows the overlap metrics of the two manual segmentations.

	GM	WM
IGC/Manual	0.593 ± 0.035	0.625 ± 0.055
InterRater	0.712 ± 0.022	0.710 ± 0.041

inhomogeneity correction and image segmentation are combined in an iterative mode. This paper presents positive results of the proposed method applied to both simulated and real brain MRIs. More solid validation and comparison with other popular brain image segmentation methods will be done in future studies.

References

1. Ashburner, J., Friston, K.J.: Unified segmentation. Neuroimage **26** (2005) 839–851
2. Boykov, Y., Veksler, O., Zabih, R.: Fast approximate energy minimization via graph cuts. IEEE Trans. Pattern Anal. Machine Intell. **23(11)** (2001) 1222–1239
3. Geman, S., Geman, D.: Stochastic relaxation, gibbs distributions, and the bayesian restoration of images. IEEE Trans. Pattern Anal. Machine Intell. **6** (1984) 721–741 classic.
4. Besag, J.: On the statistical analysis of dirty picture. J. R. Stat. Soc., B **48(3)** (1986) 259–302
5. Greig, D., Porteous, B.T., Seheult, A.H.: Exact maximum a posteriori estimation for binary images. J. R. Stat. Soc., B **2** (1989) 271–279
6. Boykov, Y., Kolmogorov, V.: An experimental comparison of min-cut/max-flow algorithms for energy minimization in vision. IEEE Trans. Pattern Anal. Machine Intell. **26** (2004) 1124–1137
7. Kolmogorov, V., Zabih, R.: What energy functions can be minimized via graph cuts? IEEE Trans. Pattern Anal. Machine Intell. **26(2)** (2004) 147–159
8. Avants, B.: Shape Optimizing Diffeomorphisms for Medical Image Analysis. PhD thesis, University of Pennsylvania (2005)
9. Rousseeuw, P.J., Leroy, A.M.: Robust Regression and Outlier Detection. New York: Wiley (1987)
10. Malik, J., Belongie, S., Leung, T., Shi, J.: Contour and texture analysis for image segmentation. International Journal of Computer Vision **43(1)** (2001) 7–27
11. Lee, S., Wolberg, G., S.Y., S.: Scattered data interpolation with multilevel b-splines. IEEE Trans. Visualization and Computer Graphics **2(4)** (1997) 337–354
12. Yan, M., Karp, J.: An adaptive bayesian approach to three dimensional mr brain segmentation. In: Proc. XIVth Int. Conf. Information Processing Medical Imaging. (1995) 201–213
13. Collins, D., Zijdenbos, A., Kollokian, V., Sled, J., Kabani, N., Holmes, C., A.C., E.: Design and construction of a realistic digital brain phantom. IEEE Trans. Med Imaging **17** (1998) 463–468